Setting up an *in vitro* system to analyze the effect of fluid pressure on the growth and morphology of pancreatic tumor cells grown in 3D

Faculty of Sciences

Final Degree Project in Biotechnology

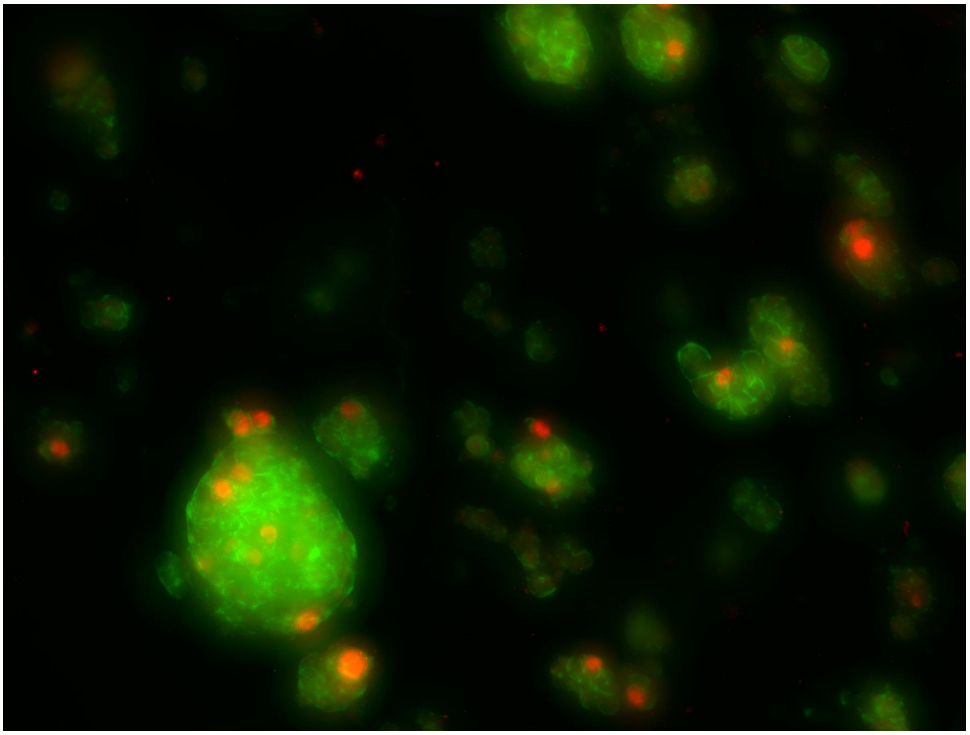

Author: Silvia Ferrer Royo

Directors: Alejandra González Loyola and José Manuel García Aznar

Academic year 2022/2023

Laboratory of Multiscale in Mechanical and Biological Engineering - I3A

INDEX

1. ABSTRACT

Up until today, pancreatic cancer is one of the deadliest and fastest-killing cancers. A late diagnosis, the lack of effective therapies and the tumor's chemoresistance are the principal causes of such elevated mortality rates. Pancreatic ductal adenocarcinoma (PDAC) is the most common type of pancreatic cancer and its noticeable resistance to chemotherapy drugs is favored by its dense stroma and high interstitial fluid pressure (IFP). In this work, it was our objective to design a system that allowed us to recreate *in vitro* the IFP to which PDAC cells are subjected and to evaluate the effect IFP has on their growth and morphology. For this purpose, we created a 3D printed system with which we were able to exert a maximum IFP of 29.3 mmHg over microfluidic 3D cultures of two PDAC cell lines (PANC-1 and PDX 354-gfp). Spheroids size, morphology, growth rate and distribution according to their area were analyzed for 3D cultures under different fluid pressure conditions. The results obtained suggested that PANC-1 cells grow better with an IFP of 29.3 mmHg but were inconclusive in regard to the PDX cell line used. Additionally, we tested the possibility of drug supply to tumorous cells grown in microchips using our 3D printed system with positive results.

2. INTRODUCTION

2.1. Pancreatic cancer

Pancreatic cancer is one of the most lethal type of cancer nowadays, representing the seventh leading cause of cancer-related deaths worldwide (1). The high mortality associated with this type of tumors is due, in many cases, to a late diagnosis. This is because non-appreciable symptoms are shown at early stages and the majority of those that appear at late stages are compatible with other diseases. This fact explains why up to 80 percent of pancreatic cancer cases are diagnosed at late stages, thus being much more difficult to be treated (2). The five-year survival rate depends on the stage and the size of the tumor. Nowadays, the combined five-year survival rate for pancreatic cancer stands at only 9%, despite new advances in development of tools for an earlier diagnosis and more knowledge of potential risk factors, such as smoking, alcohol and red meat consumption, harboring diabetes mellitus or a family history of pancreatic cancer (1).

To better understand the characteristics of pancreatic cancer, this work will begin with an introduction to the physiology of the organ, where these tumors develop. The pancreas is an elongated gland situated in the upper abdomen, behind the stomach. It has three differentiated parts: the head, the body, and the tail and two physiological functions: endocrine and exocrine (3). On the one hand, the endocrine part of the pancreas is organized in islets of Langerhans, that secrete glucagon, insulin, somatostatin, ghrelin, and pancreatic polypeptide (4), hormones that regulate blood sugar levels and appetite. On the other hand, its exocrine function consists in the production of pancreatic juice, an enzyme-rich secretion that helps in the food digestion process.

Similar to all types of cancer, pancreatic cancer is generated due to an excessive and uncontrollable proliferation of cells. When cells grow confined in a specific tissue (neoplasia) and do not spread to other locations, a benign tumor is formed. However, if cells acquire the ability to spread to other parts of the body via the lymphatic or circulatory systems (metastasis), a malignant tumor is formed. This second kind of tumors are the real cancerous ones, which get more and more difficult to treat as time goes by. Sometimes, certain benign tumors can turn into malignant tumors if treatment is not received (5)

The most common type of pancreatic cancer (around 95% of all cases) is the so-called pancreatic adenocarcinoma, which affects the exocrine cells of the pancreas. The exocrine part of the pancreas is bigger than the endocrine one, and the tumors associated affect, normally, to the ducts where the pancreatic juice is released (thus its name “pancreatic ductal adenocarcinoma”, PDAC). PDAC patients commonly suffer metastasis to the liver, lungs, peritoneum or lymph nodes (6).

Pancreatic cancer and other types of cancer have a series of common characteristics first described by Hanahan and Weinberg in 2000 and then extended by the same authors in 2011 (**fig. 1**) (7), that include:

- Self-sufficiency in growth signals
- Insensitivity to anti-growth signals
- Tissue invasion and metastasis
- Limitless replicative potential
- Evading apoptosis
- Sustained angiogenesis
- Deregulating cellular energetics
- Resisting cell death
- Avoiding immune destruction
- Genome instability and mutation

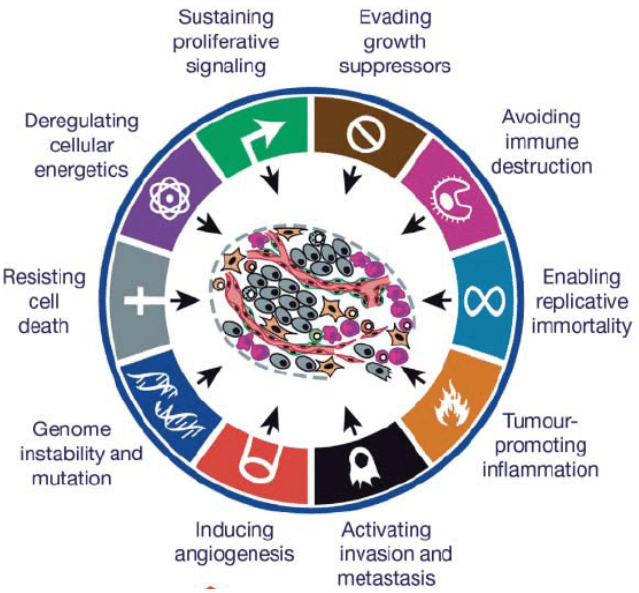

Fig. 1: Acquired capabilities of cancer suggested by Hanahan and Weinberg. Hanahan and Weinberg, 2011.

2.2. Pancreatic tumor microenvironment

The tumor microenvironment (TME) is a complex entity in constant change. It is defined as the area surrounding a tumor as well as the set of normal cells, molecules and vessels that enclose and feed cancerous cells. TME is required for tumor cells to grow, spread to other locations and colonize other organs and tissues.

As it was described by Truffi et al. (8), "TME is not just a silent bystander, but rather an active promoter of cancer progression". In fact, just as a tumor can alter its microenvironment, the TME can also have a big impact on the growth and progression of a tumor. The tumor stroma is mainly composed of fibroblasts, endothelial cells and extracellular matrix. However, its composition can vary notably from one type of tumor to another. By the secretion of different factors, stromal cells participate in tumor growth, invasion, vascularization, metastasis and drug resistance (9). Immune infiltrating cells also play an important role in tumor development. Depending on their nature, immune cells can either suppress tumor formation (e.g.,T_{CD8+} and NK cells) or promote it (e.g., T_{reg}).

Particularly, PDAC TME is characterized by a dense stroma due to the presence of numerous cancer-associated fibroblasts (CAFs) and a high heterogeneity of cellular and acellular components, between which a complex crosstalk exists (**fig. 2**). In PDAC, normal fibroblasts can act as precursors of CAFs, which play a crucial role in this type of cancer, as they facilitate the communication between cancerous cells and other components of the emerging TME (9). Pancreatic cancer stroma includes immunosuppressive cells too, such as myeloid-derived suppressor cells, tumor-associated macrophages and regulatory T cells (10, 11) . Furthermore, it is rich in stellate cells, a type of quiescent stromal cells of mesenchymal origin highly sensitive to TGF-β (transforming growth factor

beta). TGF-β promotes the transition of stellate cells from a quiescent state to an activated state . At its quiescent state, stellate cells take part in the modification of the extracellular matrix via degradation of enzymes and production of some extracellular matrix proteins (9). Once activated, they can promote angiogenesis by secreting proangiogenic factors such as VEGF-A (vascular endothelial growth factor A) and MMP-2 (matrix metalloproteinase 2) (9). PDAC is also characterized by few and collapsed blood vessels in PDAC inner tumors and afunctional lymphatic vessels.

The extracellular matrix (ECM) also plays a fundamental role in PDAC. The ECM is the principal acellular component of PDAC. It is composed of water, proteins (primarily collagen) and polysaccharides. Its function is to act as a scaffold for the surrounding cells and to regulate their behavior. In PDAC, activated CAFs contribute to the deposition of new ECM by secreting several ECM proteins like hyaluronan and collagen, which increases TME stiffness as well as solid stress. In addition, both hyaluronan and collagen (to a larger extent) have been related to the increase of constricted and collapsed vessels (12).

Overall, a great variety of cell types interact in the TME, and it is widely accepted that the microenvironment found in pancreatic cancer promotes the survival of tumorous cells, cancer progression and metastasis. In fact, new therapies for PDAC targeting features within the TME are being studied (13, 14, 15).

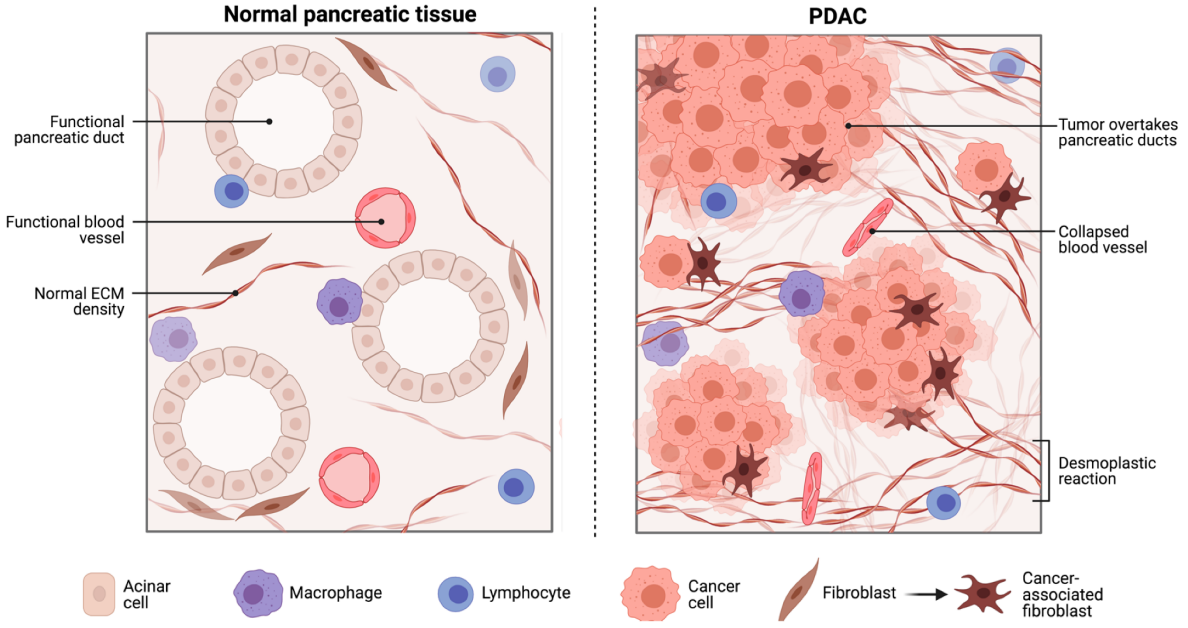

Fig. 2: Illustration showing the differences between normal pancreatic tissue and PDAC at a structural and composition level. Merali et al., 2021 (16).

2.3. Extracellular matrix and interstitial fluid pressure in PDAC

The ECM consists of a scaffold made of water, proteins and polysaccharides that determines the biochemical and biomechanical properties of the cells embedded inside. It has been proved that changes in the ECM composition can trigger the development of a malignant tumor (17).

PDAC have a dense fibrotic stroma and an ECM whose principal proteic component is collagen, specifically collagen type I (among others such as integrins, proteases, glycoproteins, etc. that can all interact with cancerous cells). The dense and complex PDAC ECM constitutes a physical barrier for chemotherapy drugs against the tumor, which reduces the efficacy of those drugs. The

two main players that contribute to PDAC aggressiveness are cancer stem cells and the TME composed by cancer associated fibroblasts, immunosuppressive immune cells and a dense extracellular matrix . The sparse and permeable blood vessels (BVs), the lack of functional lymphatic vessels (LVs) and the residual stresses generated by the ECM (as a consequence of irregular tumor growth) have been postulated as the cause of the elevated interstitial fluid pressure (IFP) found in PDAC due to fluids excess. Solid tumors generally show a higher IFP than normal tissues (increments of 4-50 mmHg compared to normal surrounding tissues had been measured for different types of cancer (18, 19). The high IFP and residual stress induce BV compression and thus, chemotherapy delivery in the tumor is severely impaired, which reduces the efficacy of chemotherapy drugs (20).

In particular, in the case of PDAC, the abundance of hyaluronan has been reported to elevate the IFP (21, 22) and in some autochthonous PDAC, values of IFP ranging from 75 to 130 mmHg have been obtained (21) .

2.4. 3D cell culture in microfluidic devices

3D cultures mimic tissue and organ structures in a more physiological way than 2D cultures do. And at the same time 3D cultures are more similar to *in vivo* models since they preserve the cell morphology and molecular mechanisms and show proper cell-cell and cell-environment interactions (23).

Microfluidic technology, which started in the early 1980s (24), has experimented an unprecedented growth in recent years. This includes the manufacture of miniaturized devices with microchannels and chambers through which fluids can flow or rest confined (microchips), as well as the study of the fluids' behavior inside microchips. Some of the most recent applications of microfluidic devices include organ-on-chip experiments, preclinical assays, drug-based studies, disease diagnosis and droplet-based microfluidics. There are several reasons to choose microfluidic devices while working with 3D cell cultures:

- Precise control over fluids
- Easy handling
- Flexibility and customization of microfluidic devices design
- Microchips attached to glass bottom dishes (with their respective lids) serve as sterile units
- Micrometre-sized spaces, make it easier to mimic and control factors that are determinant for the microenvironment
- Co-cultures can be performed in microchips
- Transparency makes them suitable for live microscopy
- Small sample, medium and reagents volumes are required, which helps reduce assay costs

3. SCIENTIFIC BACKGROUND

Over the last decade, multiple strategies targeting CAFs or ECM in PDAC have been assayed without success (25, 26). This scenario highlights the urgent need to develop innovative experimental therapies to restrain PDAC progression.

PDAC harbors one of the most complex solid TME, where the elevated IFP and residual stress act as barrier to drug delivery and contributes to the expansion of metastatic cells via lymphatic draining (27). Although the relevance of high IFP in PDAC is widely accepted, as far as we are concerned, no assays have determined the effects of IFP on pancreatic tumor cells at morphological, structural and growth levels. In view of this situation, our project arose.

The ultimate aim of our project is to recreate *in vitro* the pressure that interstitial fluid would be exerting over cancerous cells in PDAC in order to evaluate the effects of IFP on the growth and morphology of the cells. We achieved this goal by applying an external fluid pressure with a 3D printed system over a microfluidic 3D culture of an established human tumor pancreatic cell line (PANC-1 cells). Thus, if we understand the TME mechanical mechanisms that regulate tumor growth we could design future target therapeutic strategies against PDAC.

Common methods to apply hydrostatic pressure to cell cultures consist of connecting an external liquid reservoir, a glass column filled with culture medium or a syringe pump to the cell culture dishes (19, 28). Prior to the method described on this memory, we tried to connect our microfluidic devices to glass columns filled with medium. However, the material used to make the microchips was not resistant enough to support the columns weight and the microchips detached from the surface they were attached to. We also tried to replace the glass columns with 5 mL plastic syringes, but the pressure obtained at the base of the syringes was not large enough to be compared with the pressure pancreatic cells can undergo inside a tumor.

The closest approach to our pressure application system was the one described by Shang et al. in 2021 (29), that we used as a basis to build our prototypes. Finally, with the aid of our 3D printed system, we were able to apply a maximum pressure of 29.3 mmHg over the cultures (see 3D impression and fabrication of the first and second prototypes section).

4. AIMS AND OBJECTIVES OF THE FINAL DEGREE PROJECT

1. Set up the conditions for a pancreatic-on-a-chip model using human pancreatic tumor spheroids grown in a microfluidic device developed in the lab using different concentrations of extracellular matrix (collagen) for their 3D growth.
2. Establish a procedure to induce interstitial fluid pressure in our pancreatic-on-a-chip model.
3. Determine the effects of interstitial fluid pressure on the pancreatic tumor spheroids at morphological and growth level.
4. Study if the interstitial fluid pressure effects observed in human pancreatic tumor spheroids derived from patients are the same as with an established human tumor cell line.

5. MATERIALS AND METHODS

5.1. Microfluidic devices fabrication

Microdevices were used according to the fabrication methodology described by Shin et al. (30). The desired geometry was achieved by using soft lithography to create relief patterns in a silicon wafer. The geometry of the devices was based on the one used by Farahat et al. (31), which consists of a central chamber that contains the cells embedded in a hydrogel connected to two media channels for nutrients and growth factors supply. The designs were manufactured externally at INA (Aragon Nanoscience Institute). Replicates of this micropattern were obtained by using polydimethylsiloxane (PDMS). PDMS is a type of silicone widely used in microfluidic research because of its particular properties, such as biocompatibility, gas permeability, transparency (needed for microscopy studies) and low cost compared to other *in vitro* models (due to its micrometric scale). All 3D cell cultures used for the experiments performed in this TFG were grown in polydimethylsiloxane (PDMS) microchips fabricated at M2BE lab (I3A's laboratories).

The fabrication of the microchips lasted 4 working days. Thus, during the first day, wafers served as a mold to cure PDMS (Sylgard 184, Dow Corning GmbH) in a 10:1 ratio (base elastomer and a curing agent) to obtain the desired geometry. The wafers were then cured in an oven at 80ºC for 24 hours. During the second day, the resulting PDMS wafers were trimmed and perforated with different diameters in order to create our final microdevices (**fig. 3**).

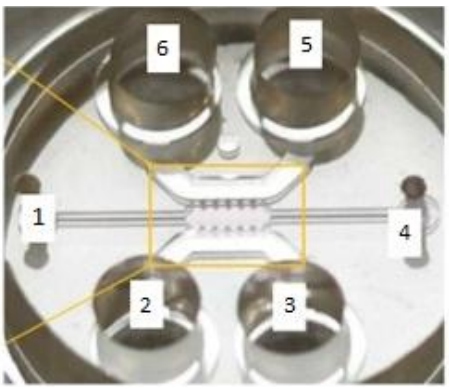

Fig. 3: Photograph of the wells of one of the microchips used. Wells 1 and 4 (for hydrogel loading) have a diameter of 1 mm while wells 2, 3, 5 and 6 have a diameter of 3 mm (for media supply). The orange rectangle shows the central chamber where cells are seeded. Plou et al., 2018 (32).

Once the microchips were obtained, all of the excess PDMS was removed and the devices were sterilized in an autoclave machine. Next, chips were dried out inside an oven at 80ºC for 24 hours. Following those 24 hours, an oxygen plasma treatment was performed to attach the PDMS microchips to glass bottom dishes (400µ-Dish 35mm High Glass Bottom, Ibidi). PDMS requires this treatment to tightly bond with glass surfaces. For that, both microchips with the geometry faced up and opened glass bottom dishes were placed inside an oxygen plasma machine for two minutes. During this time, hydrocarbon groups from the PDMS were removed and hydrophilic -OH groups were exposed. Thus, when the devices were placed on top of the glass bottom dishes and gently press, covalent bonds were formed between -OH groups of the PDMS and silicon atoms of the glass (Si-O-Si). Quickly after attaching the devices to the glass surface, they were treated with a 2 mg/mL polydopamine (PDA) solution to improve surface-matrix attachment. PDA helps to modify the surface of microfluidic devices, since although plasma treatment renders PDMS hydrophilic, the effect is only temporary. The addition of a PDA coat on top of PDMS reduces the static water contact angle from about 120° to 20°–100°, which means the pressure required to pump an aqueous solution through the PDMS channels is considerably reduced (33). Additionally, the adhesion of cells onto PDMS can be improved with this treatment, as PDA can interact with amine groups of extracellular matrix proteins such as collagen (34). After the PDA treatment, channels were washed twice with distilled water and the dishes with the devices were placed in the oven at 60ºC for 24 hours. After this time, the microchips are placed at room temperature and used to culture cells within 2 weeks.

5.2. 3D impression and fabrication of the first and second prototypes

With the objective of simulating the IFP that cancerous cells undergo inside a tumor, we designed an initial prototype that reminds of a dropper, based on the one developed by Shang et al. (29). It consisted of a construction formed by different 3D printed pieces that sustained 5 mL syringes full of culture medium that connected with the microchip medium reservoirs via silicone tubes also full of culture medium. The height between the microchips and the syringes could be modified so that the effect of different hydrostatic pressure values on cell growth could be tested.

Initially, we wanted to test the effect of hydrostatic pressure conditions that correspond to medium columns of 10, 20 and 40 cm, according to the equation $\mathbf{P = h\rho g}$, were P is pressure, h is height of the column, ρ is density of the liquid and g is the gravitational field strength. However, with this first prototype that was later substituted by an improved more stable one, we were only able to

test the effect of hydrostatic pressure conditions that correspond to medium columns whose height was 10 and 40 cm. The pressure applied in each case was calculated as follows:

10 cm columns: $P = h\rho g \rightarrow h_{Hg} \times \rho_{Hg} \times g = h_{DMEM} \times \rho_{DMEM} \times g \rightarrow h_{Hg} = (\rho_{DMEM}/\rho_{Hg}) \times h_{DMEM}$
$\rightarrow \mathbf{h_{Hg}} = (0{,}99 \div 13{,}5) \times 100 = \mathbf{7{,}3\ mmHg}$

40 cm columns: $P = h\rho g \rightarrow h_{Hg} \times \rho_{Hg} \times g = h_{DMEM} \times \rho_{DMEM} \times g \rightarrow h_{Hg} = (\rho_{DMEM}/\rho_{Hg}) \times h_{DMEM}$
$\rightarrow \mathbf{h_{Hg}} = (0{,}99 \div 13{,}5) \times 400 = \mathbf{29{,}3\ mmHg}$

DMEM density was calculated using a straight-line pattern created from measures of the weight of different DMEM volumes.

Therefore, we created two different types of sets: a shorter one for the 10 cm columns and a larger one for the 40 cm columns (fig. 4). Each set was composed of:

- A base of 6 × 10 cm that had a central circle-shaped hole to place the glass bottom dish with the microdevice on it and four square-shaped hole, one on each corner, to insert the pillars.
- Four pillars that were attached to the base. The majority of the pillars were 19 cm long and had holes every centimeter so that height could be regulated. For the shortest set, only one set of four of these columns was required to create a structure that reached 10 cm height. However, for the largest set we used a total of twelve to reach 40 cm height: two 19 cm pillars and one 8cm pillar on each corner, attached to one another.
- Two locking pins that were inserted into the pillars' holes at the desired height.
- Two pieces with two square-shaped holes at the extremes in order to fit into two pillars and connect them and two circle-shaped holes in the middle where the syringes were inserted.

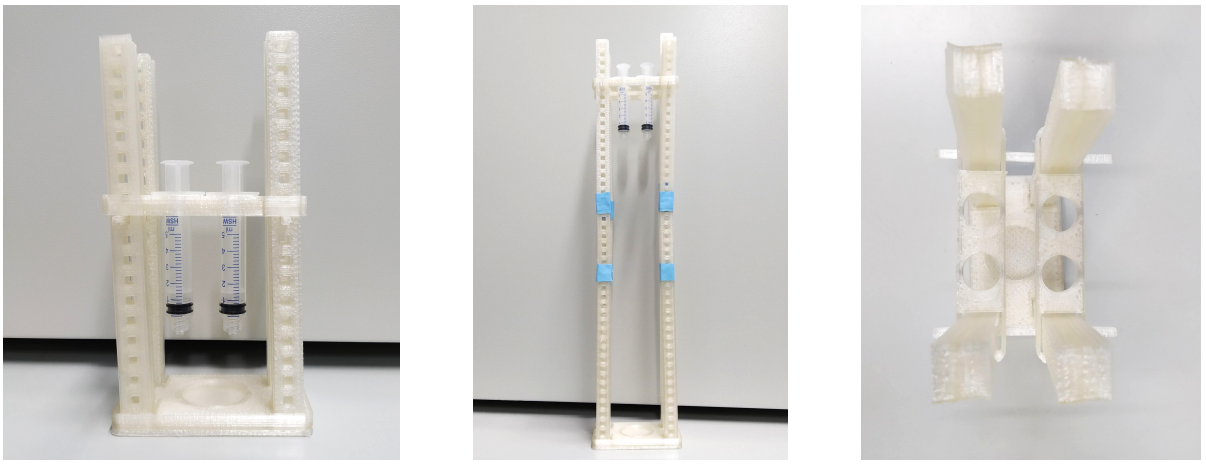

Fig. 4: Images of the first 3D printed prototypes: front view of the 10 cm set with syringes (left), front view of the 40 cm set with syringes (right) and top view of both sets showing the holes where syringes were inserted (middle).

All of the pieces used for this first prototype were printed using the NX Pro Pellets 3D printer (Tumaker) that is owned by the M2BE laboratory. NX Pro Pellets printer works by melting pellets of a certain material and depositing the melted product on the platform or heated bed. The material used was polylactic acid (PLA), a thermoplastic polymer formed after polymerization of lactic acid molecules. It is widely used in biomedicine and tissue engineering due to its good mechanical and biological properties like its biocompatibility, biodegradability and the fact that the degradation product obtained after several enzymatic reactions (lactic acid) is safe.

The designs of each one of the structures were kindly created by Pablo Martín Compaired in a specific informatic format that was later imported to the Simplify3D program (Version 4.1.2; Simplify 3D LLC: 2019), which was the program that we used to control the 3D printer in the laboratory. Different parameters that affect the printing process can be modified through Simplify3D, the ones that we selected were the ones that follow:

- Printing diameter: 0,4 mm
- Temperature of the heated bed: 45ºC
- Printing temperature: 200ºC
- Infill density: 100% (which means that the material is completely solid, there are no hollow parts)
- Impression speed: 3000 mm/min
- Print speed: 7000 mm/min
- Retraction distance: 4,5 mm
- Vertical retraction lift: 0,6 mm

With these settings, a ".gcode" file was created and later executed by the 3D printer. Using this system we were able to recreate the IFP we wanted, but during the assembling process we realize that the system was highly unstable, partially because the pillars required for the largest set had not been glued together before, so we needed to use far more adhesive tape that we wanted. But also because the finishing of the pieces was not perfect, some pieces had little nicks or burrs so they did not fit perfectly into each other. In fact, after the pieces were printed, especially the pillars, we spent some time filing them and removing excess material. Due to the reasons explained above, we decided to try a second prototype also designed by Pablo Martín Compaired which was definitely more stable and efficient. The reason for its stability was the addition of a mechanism similar to the one of nuts and bolts to connect the base with the pillars and one pillar to each other.

Fig. 5: Images of the second and final 3D printed prototypes: front view of the 10 cm set with syringes (left), front view of the 40 cm set with syringes (right) and top view of both sets showing the holes where syringes were inserted (middle).

All pieces made up with this second prototype were created using the printer Ender-3 S1 Pro (Creality) and the following settings were selected:

- Temperature of the heated bed: 60ºC
- Printing temperature: 210ºC
- Infill density: 20%

- Print speed: 50 mm/s
- Travel speed: 120 mm/s
- Retraction speed: 40 mm/s
- Retraction distance: 0,8 mm

It is remarkable that the material used for this second printing were filaments of black PLA (PLA+ by the company eSUN) reinforced to improve its toughness and layer adhesion compared to the white PLA used for the first prototype. Each set consisted of a 7×11 cm base with a circle-shaped hole to insert the microchips, four pillars, two locking pins and a rectangular piece on top with four circle-shaped holes in the middle to insert the syringes (fig. 5).

5.3. Cell culture

In this work, two cell lines were used: the human commercial cell line PANC-1 (https://www.atcc.org/products/crl-1469) and an established PDX cell line (354-gfp).

PANC-1 was the cell line chosen to carry out most of the experiments. PANC-1 is a human epithelioid cell line established from a pancreatic ductal adenocarcinoma from a 56-year-old Caucasian male. They are adherent cells, however spheroids can be generated from an initial PANC-1 cell culture, as explained in the following paragraph. This human cell line has been used worldwide as an in vitro model to study PDAC carcinogenesis, the development of new therapies for this type of cancer and the role of the intermediate filament keratin reorganization on the alignment and migration of cancer cells, among others (35, 36).

The PDX cell line used in this work was obtained thanks to a collaboration of the hosting lab with the laboratory of Patricia Sancho at Miguel Servet Hospital. PDX cells (the acronym for patient-derived xenografts cells) are cancerous cells obtained through tumor tissue engraftment. For that purpose, human cancer tissues are transplanted into humanized or immunocompromised mice (37) . Particularly, these PDX 354-gfp are characterized by its aggressiveness, mesenchymal state and sensitivity to pH.

We performed two types of cultures using the above mentioned cell lines. Firstly, a 2D culture in which the cells grew adhered to the surface of a T-25 flask in complete DMEM medium (Dulbecco's Modified Eagle Medium) supplemented with fetal bovine serum (FBS), penicillin and streptomycin. Secondly, a 3D culture in which cells coming from 2D culture were allowed to grow in suspension forming spheroids. This 3D culture required T-25 flasks with a coat of poli(2-hydroxyethyl methacrylate) (PHEMA) at the bottom of the flask to prevent cell attachment to the culture ware. Thus, allowing cells growing in suspension as spheres. The medium used in this case was DMEM/F-12 (Dulbecco's Modified Eagle Medium/Nutrient Mixture F-12), also supplemented with FBS, penicillin and streptomycin. Cell passaging was performed when needed till maximum passage 20.

5.4. Hydrogel preparation

The day after the microchips PDA treatment (see microfluidic devices fabrication section), spheroids embedded in collagen hydrogel were added into the central channel of the microchip at a cell density of $5{,}4 \times 10^5$ cells/mL . For that, a 3D spheres cell culture of PANC-1 cell line was resuspended until homogeneity and cell density was determined after placing 10 µL of the culture in a Neubauer chamber and counting the number of cells observed in each one of the four large corner squares. The formula used to calculate cell density was the following:

$$\textbf{Cell density (cells/mL)} = \textbf{nº cells counted} \times 10^4 / \textbf{nº squares}$$

Then, the result was multiplied by the number of milliliters of the culture to calculate the total number of cells. After that, cells were centrifuged. The supernatant was discarded and the pellet was resuspended in the appropriate volume of DMEM/F-12 to have a final cell density of 10^6 cells/mL.

Thereupon, hydrogels were prepared to be placed into the central channel. Hydrogels were fabricated from a stock of rat tail type I collagen (BD Bioscience, San Jose, USA), diluted to the final desired collagen concentration using 10x phosphate buffered saline (PBS), DMEM/F-12 and 0.5 NaOH solution. The pH of all the resulting hydrogels was 7. The temperature of all the components was kept at 4℃ during the entire hydrogel fabrication process. The final cell density within those hydrogels was 5×10^5 cells/mL and collagen was added at a final concentration of 4 mg/mL or 6 mg/mL (we tested two different conditions for some experiments). After the solution was added, microchips were polymerized in humid chambers at 37ºC, being turned upside down every 5 minutes for 20 minutes to ensure homogenous dissemination of cells through the hydrogel while polymerizing, and also to prevent cells from transferring onto top or bottom surfaces and consequent 2D growth. Then media channel reservoirs were filled with DMEM/F-12 to ensure nutrient supply. Finally, glass bottom dishes with the microchips inside were closed with their respective sterilized lids and incubated at 37ºC.

The following day, photographs of the central chamber of all of the devices were taken prior to any manipulation to later compare them with the photographs taken on the last day of the experiment in order to evaluate cellular growth and morphology. Photographs of control cells were taken on days 1, 3, 5, 7 and 9 after seeding. Medium was changed every two days.

Microchips in which pressure was going to be applied were placed in the central circle-shaped hole of the 3D printed structure reserved for them (see 3D impression and fabrication section) and the media reservoirs were connected with four syringes full of DMEM/F-12 medium through silicone tubes full of medium. Photographs of cells under pressure were taken on days 1 (prior to fluid pressure) and on day 6 after fluid pressure, when the structures were dismantled. To make sure that neither medium or cells escaped the microchips in case any accident happened and the silicone tubes had no option to pop out of the medium reservoirs, a coat of sterile glue was applied covering the devices entirely. This glue was gently removed on day six with the aid of some tweezers, so that pictures could be taken.

5.5. Bright-field microscopy, immunofluorescence staining and image acquisition

Bright-field pictures of the central chamber of each set of microchips were taken on days 1, 3, 5, 7 and 9 after seeding (control chips) or on day 1 after seeding and on the last cell culture day, when the structures were dismantled (chips under fluid pressure and its respective control chips), using the inverted microscope Leica Dmi1 connected to a computer and a camera. The computer program used to visualize the 3D cultures and take pictures was Phyton Viewer. Then, chips were fixed with paraformaldehyde and kept at 4ºC with PBS-azide to prevent microbial contamination. Like that, they could be saved in refrigeration for weeks.

Chips saved in refrigeration were later stained for fluorescence microscopy. The fluorescent staining procedure took 3 days. During the first day, chips were washed with PBS-azide (which serves as a preservative and storage buffer) before cell membranes were permeabilized with 0,1% Triton X-100. After that, chips were washed twice with a PBS-azide solution and left in the fridge overnight with 5% BSA. During the second day, the 5% BSA solution was removed from the chips and a solution

containing 0,5% BSA, 0,2% Triton X-100 and two primary antibodies in proportion 1:200 (anti-Ki-67 and anti-Sox9) was added. Chips with this solution were left in the fridge overnight. During the third day, chips were washed three times with PBS-azide before adding a solution containing 0,5% BSA, 0,2% Triton X-100, DAPI (1:100), phalloidin (1:200) and two secondary antibodies in proportion 1:200. The devices were incubated for 4 hours at room temperature in the dark. Afterwards, they were washed twice with PBS-azide and saved at 4ºC in the dark.

Fluorescence microscopy images were captured using the microscope Axio Observer 7 (ZEISS) and the software ZEN 3.5 (blue edition) and analyzed using FIJI software. Three pictures of different regions of the central chamber of each microchip were taken. The purpose of the staining used is explained below.

- DAPI (4′,6-diamidino-2-phenylindole) is a blue fluorescent stain that binds strongly to adenine and thymine rich DNA regions and thus, dyes cell nuclei.
- Phalloidin is a bicycle heptapeptide that binds to actin filaments and allows to distinguish the plasma membrane as it is conjugated with a bright red dye (Alexa Fluor™ 594) that stains the layer of actin filaments that is found underneath it in animal cells.
- Ki-67 is a nuclear protein that serves as a biomarker of cell proliferation. It can be found during all active phases of the cell cycle, but is absent from resting cells (G_0) (38) . To evaluate its expression in our spheroids we used a primary anti-Ki-67 mouse antibody and a secondary goat anti-mouse IgG conjugated with the near-infrared-fluorescent dye Alexa Fluor™ 647
- Sox9 is a transcription factor involved in pancreas organogenesis that is upregulated in the majority of PDAC cases (39) . It is commonly used as a biomarker for pancreatic stem cells, although it is also expressed in other cell types like astrocytes and epithelial lung cells. To evaluate its expression, we used a primary anti-Sox9 rabbit antibody and a secondary goat anti-rabbit IgG conjugated with the green-fluorescent dye Alexa Fluor™ 488.

5.6. Image analysis

The bright-field pictures of the central chamber of the microchips were analyzed with ImageJ, which is a public domain Java image processing program. ImageJ was used to measure the areas of the spheroids and to calculate their growth under determined conditions during the time period considered between the day after seeding and the final cell culture day (see cell culture and hydrogel preparation section). For that, in each microchip the perimeter of a number of spheroids between 40 to 50 distributed all along the central chamber was marked on day 1 after seeding and on the last cell culture day. For each spheroid, the program returns a series of measurements that includes its area, standard deviation, mean gray value and minimum and maximum gray values. With the data obtained from ImageJ, an Excel document for each chip was created. The document includes the initial and final area of each spheroid and the ratio **Area spheroid nºx on the last cell culture day/Area spheroid nºx on day 1**, that we named “growth ratio”.

Fluorescence microscopy images were analyzed with the image processing software FIJI. For each picture, we counted the number of spheroids and cells positive for Ki67 (proliferative cells) and measured the area of all the spheroids that could be distinguished. With those values we were able to calculate the ratio **Nº of positive cells for Ki67 in an spheroid/Area of the spheroid**, that we named “proliferation ratio”. We also quantified the intensity of phalloidin of each spheroid through

its mean gray value (mean pixel intensity in the phalloidin channel). This data corresponds with the average actin intensity in the spheroids.

5.7. Statistical analysis

Data analysis and graphs were created using GraphPad Prism 8 program. The number of microchips analyzed is indicated for each image in the figure legends. For *in vitro* experiments comparing spheroid growth with 4 mg/mL collagen and 6 mg/mL collagen or spheroid growth with and without fluid pressure being applied, normality tests and two-tailed unpaired Student's *t* test were performed to determine statistical significance between two means. In the instance data did not conform to normality, the nonparametrical Mann-Whitney test was performed. For *in vitro* experiments comparing growth ratios between spheroids under different fluid pressure and distribution graphs, we used two-way ANOVA test followed by Tukey's multiple comparisons test. Scattered dot plot data are shown as means ± SD, where each single dot represents an individual microchip. *P* value is stated in each figure. Differences were considered statistically significant at $P < 0.05$.

6. RESULTS AND DISCUSSION

Unlike the majority of the current studies that include spheroid culture inside microchips, in all of the experiments described, cells were introduced into the devices when spheroids were already formed. This allowed us to evaluate the effect of fluid pressure on spheroids from the beginning and reduced cell culture time inside microchips as we did not have to wait for cellular aggregation to occur.

6.1. PANC-1 spheroids grow better in 4 mg/mL collagen than in 6 mg/mL collagen

Growth and morphology of the spheroids of six microchips under each condition were evaluated.

As shown in **tables 1, 2 and 3** (annexes) and **fig. 6 and 7**, spheroids grew faster with a concentration of collagen of 4 mg/mL already at day 1 after seeding (the average area of spheroids embedded in the hydrogel with 4 mg/mL collagen was approximately twice as big as the average area of spheroids embedded in the hydrogel with 6 mg/mL collagen (**fig. 8A and 8B**)). This is why although growth ratios for both conditions were similar, spheroids grown in 4 mg/mL collagen were clearly bigger at any time compared to the ones grown in 6 mg/mL collagen. According to that, at day 6 after seeding, the majority of spheroids grown in 4 mg/mL collagen presented a size within the large ranges of area, while the majority of spheroids grown in 6 mg/mL presented a size within the small ranges of area (**fig. 8C**). This led us to think that PANC-1 cells grow faster in hydrogels that are not too stiff, since stiffness increases proportionally to collagen concentration. However, these conditions may vary from different types of spheroids. For example, as shown in an article published by Charoen et al. (40), bone cancer spheroids (U2OS cells) demonstrated better growth in 3-4 mg/mL collagen compared both weaker and stiffer collagen gels, while breast cancer spheroids (MDA-MB 231 cells) demonstrated best growth in 2 mg/mL collagen gels. Another work using breast cancer spheroids (NCI-H1299 cells) released in 2018 by Plou et al. (32) showed that spheroid growth was dependent on collagen gel concentration, being stiffer hydrogels related with lower single cell migration and with the formation of multicellular clusters that grew confined and presented a rounded morphology.

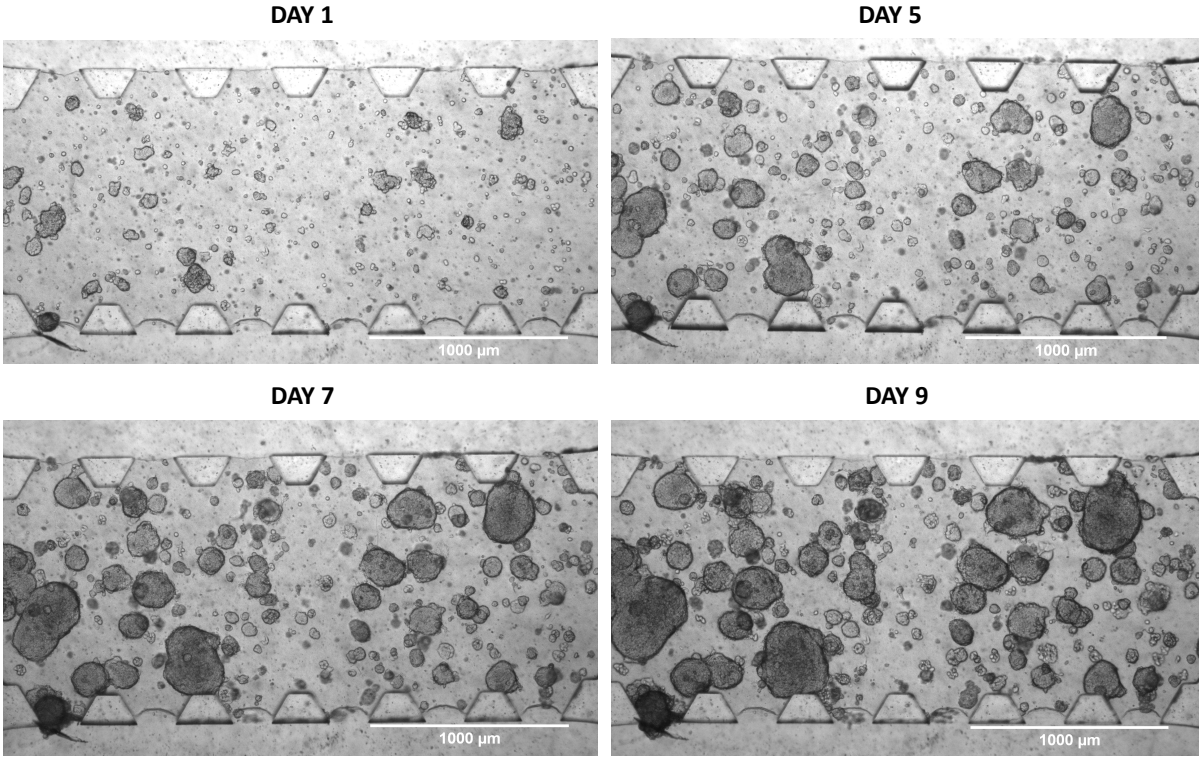

Fig. 6: Bright-field microscopy images of the central chamber of one of the microchips whose hydrogel was prepared with a concentration of collagen of 4 mg/mL at day 1 (top left), day 5 (top right), day 7 (bottom left) and day 9 (bottom right) after seeding.

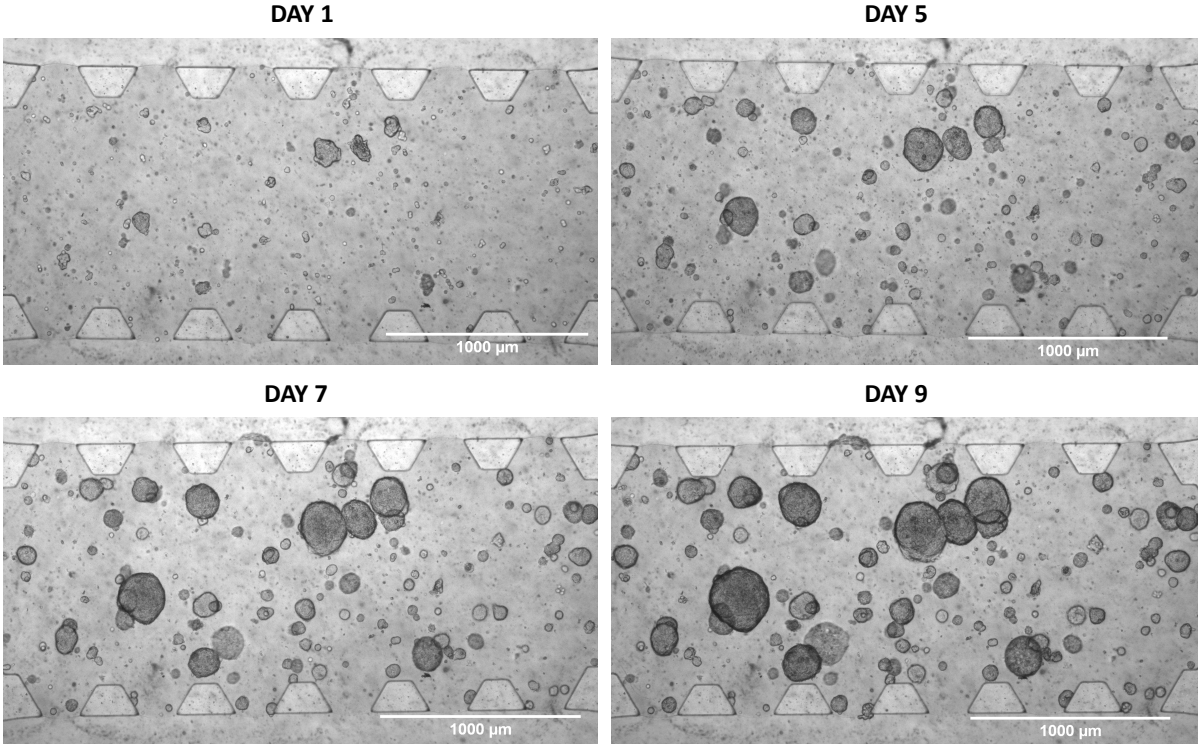

Fig. 7: Bright-field microscopy images of the central chamber of one of the microchips whose hydrogel was prepared with a concentration of collagen of 6 mg/mL at day 1 (top left), day 5 (top right), day 7 (bottom left) and day 9 (bottom right) after seeding.

We also noticed that the spheroids grown in 6 mg/mL collagen (**fig. 7**) were slightly rounder than the ones grown with a lower collagen concentration (**fig. 6**). This result matches with the observations of an article published in January of 2022 by Rodrigo et al. in which the influence of type I collagen over 3D structure and behavior of glioblastoma spheroid models was studied. This study showed that an increase in collagen concentration generated a driving force that led to cell compaction and rounder spheroids (41).

As it can be seen in **fig. 6**, at 4 mg/mL of collagen, at day 9 after seeding some spheroids grew too much to be differentiated from one another and be tracked individually from day 1 after seeding. This is the reason why we decided to carry out the following experiments using a concentration of collagen type I of 4 mg/mL (so that spheroid growth was faster and we could complete a higher number of experiments) and we decided to finish the experiments at day 6 after seeding to reduce spheroid overgrowth.

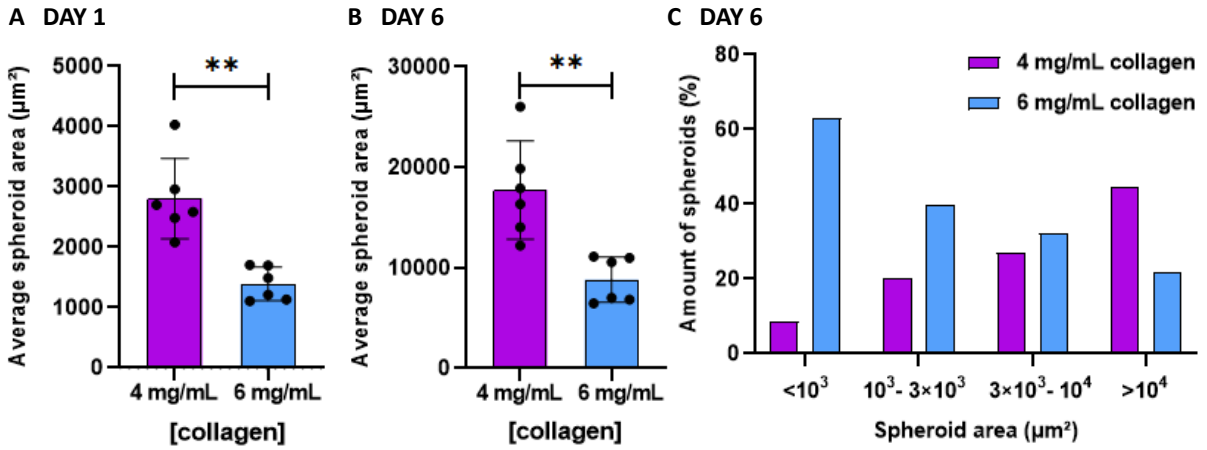

Fig. 8: **A**: Graph showing the average area of PANC-1 spheroids grown in 4 mg/mL and 6 mg/mL collagen at day 1 after seeding. Statistical analyses were performed using Mann-Whitney test. n=12 (6 chips per condition). P=0,0022. Data are means ± SD. **B** : Graph showing the average area of PANC-1 spheroids grown in 4 mg/mL and 6 mg/mL collagen at day 6 after seeding. Statistical analyses were performed using Mann-Whitney test. n=12 (6 chips per condition). P=0,0022. Data are means ± SD. **C**: Distribution graph of PANC-1 spheroids grown in 4 mg/mL and 6 mg/mL collagen according to their areas at day 6 after seeding. n=511 (225 spheroids in 4 mg/mL collagen and 286 spheroids in 6 mg/mL collagen). n.s. not significant. Data are means ± SD. All graphs were created with GraphPad Prism 8.

6.2. PANC-1 spheroids grow better with an applied fluid pressure of 29.3 mmHg

6.2.1. Results obtained from bright-field microscopy images

As described previously, thanks to our 3D printed structures, we were able to reach pressures of 7.3 mmHg and 29.3 mmHg at the base of our columns, where the microchips were placed. Structures were dismantled on day 6 after seeding and analyzed as described in the materials and methods section. We were able to analyze 6 control chips, 5 chips under an IFP of 7.3 mmHg and 4 chips under an IFP of 29.3 mmHg (initially we prepared more chips but due to unexpected events during the procedure we could only reliably analyze the chips mentioned).

As shown in **tables 4, 5 and 6** (annexes) and **fig. 9**, there is a tendency of larger average spheroid areas for microchips under IFP at day 6 after seeding. A significant difference between the mean area of control spheroids and the mean area of spheroids under an IFP of 29.3 mmHg was observed. As **table 7** (annexes) and **fig. 9** illustrate, the majority of control spheroids showed a lower growth ratio (from <2 to 3) than spheroids under IFP (especially than spheroids under a pressure of 29.3 mmHg). The group under an IFP of 29.3 mmHg showed the lowest percentage of spheroids with

a growth ratio under 2 and slightly superior percentages to the other two groups in all of the other growth ratio categories.

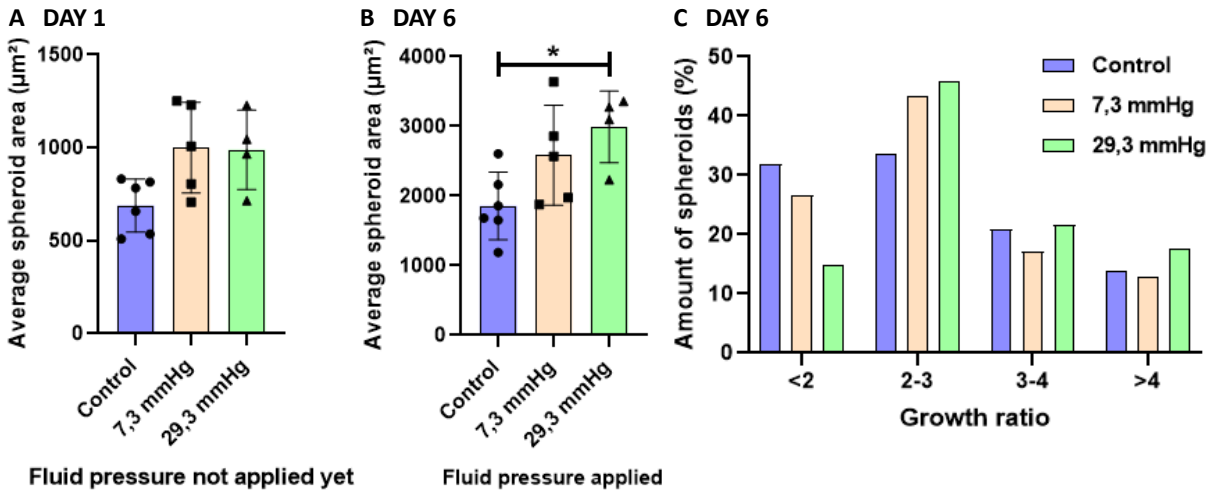

Fig. 9: **A**: Graph showing the average area of PANC-1 control spheroids and spheroids under an interstitial fluid pressure of 7.3 mmHg and 29.3 mmHg at day 1 after seeding. Statistical analyses were performed using one-way ANOVA test followed by Tukey's multiple comparisons test. n=15 (6 control chips, 5 chips under an IFP of 7.3 mmHg and 4 chips under an IFP of 29.3 mmHg). n.s. not significant. Data are means ± SD. **B**: Graph showing the average area of PANC-1 control spheroids and spheroids under an interstitial fluid pressure of 7.3 mmHg and 29.3 mmHg at day 6 after seeding. Statistical analyses were performed using one-way ANOVA test followed by Tukey's multiple comparisons test. n=15 (6 control chips, 5 chips under an IFP of 7.3 mmHg and 4 chips under an IFP of 29.3 mmHg). P=0,0263. Data are means ± SD. **C**: Distribution graph of spheroids according to their growth ratio at day 6 after seeding. Statistical analyses were performed using two-way ANOVA test followed by Tukey's multiple comparisons test. n=733 (299 control spheroids, 240 spheroids under an IFP of 7.3 mmHg and 194 spheroids under an IFP of 29.3 mmHg). n.s. not significant. Data are means ± SD. All graphs were created with GraphPad Prism 8.

We also analyzed the distribution of spheroid areas at day 1 and 6 after seeding for all chips (**fig. 10** and **tables 8 and 9** (annexes)). As expected, at day 1 after seeding (when pressure had not been applied yet) there were no significant differences within each range of area between the amount of spheroids that were later going to serve as controls or will have a certain fluid pressure applied. However, on day 6 after seeding, it was noticeable that the amount of control spheroids corresponding to the larger ranges of area was smaller than the amount of spheroids under pressure (7.3 mmHg and 29.3 mmHg) for those ranges.

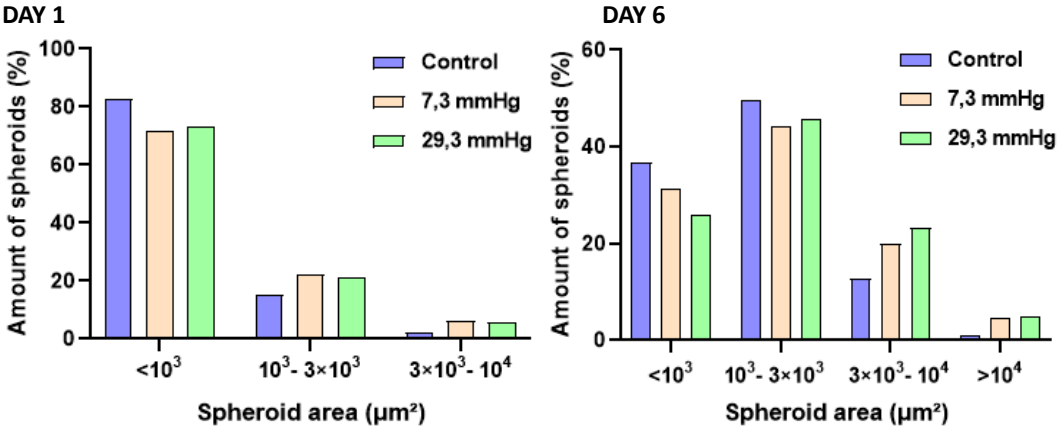

Fig. 10: Distribution graphs of PANC-1 spheroids according to their areas at day 1 (left) and day 6 (right) after seeding. Statistical analyses were performed using two-way ANOVA test followed by Tukey's multiple comparisons test. n= 733 (299 control spheroids, 240 spheroids under an IFP of 7.3 mmHg and 194 spheroids

under an IFP of 29.3 mmHg). n.s. not significant. Data are means ± SD. Graphs were created with GraphPad Prism 8.

Additionally, while taking bright-field pictures of the central chamber of the microchips on day 6 after seeding, we observed that without changing brightness and contrast parameters, a good amount of spheroids of half of the control chips seemed darker than other spheroids that were prior evaluated. Particularly, in those chips it was impossible to distinguish the cells that made up the biggest spheroids, although the spheroid area was still able to be measured. We also noticed this phenomenon to a lesser extent in a few spheroids of a couple of chips under an IFP of 7.3 mmHg (fig. 11). Because very few spheroids under an IFP of 7.3 mmHg with these characteristics were observed and not a single one under an IFP of 29.3 mmHg, we came to the conclusion that this phenomenon could be due to cellular death inside the spheroids affected and that the application of fluid pressure (within an acceptable range) could help PANC-1 cells to proliferate and survive. In order to verify this observation, immunostainings for proliferation were performed on the control and fluid pressure treated chips (as explained in bright-field microscopy, immunofluorescence staining and image acquisition section).

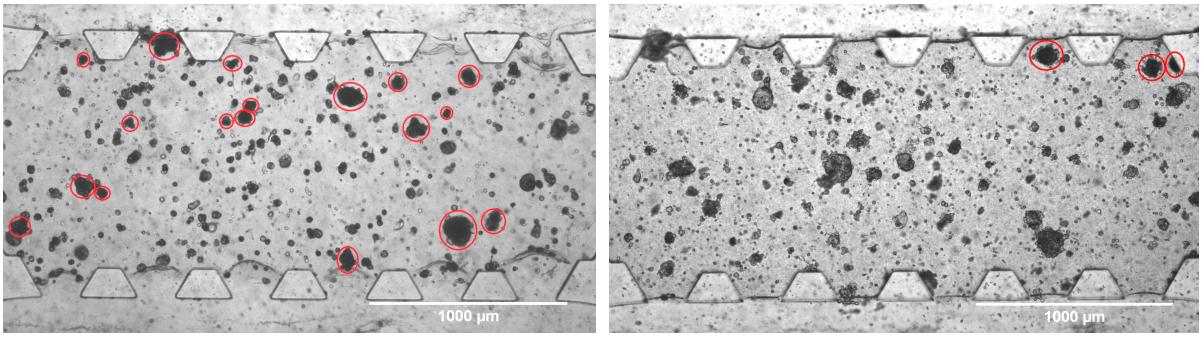

Fig. 11: Bright-field microscopy images of the central chamber of a control chip (left) and a chip that had been under an IFP of 7.3 mmHg for 5 days (right). Opaque and darker spheroids are circled in red.

6.2.2. Results obtained from fluorescence microscopy images

Fluorescence microscopy images obtained from the immunostainings were analyzed with FIJI. Channels of color composite images were splitted so that we could keep separate images (channels) for each one of the stains used. For each picture, we counted the number of spheroids and cells positive for Ki67 and measured the area of all the spheroids that could be distinguished. Then, we calculated the proliferation ratio for the positive spheroids (Nº of positive cells for Ki67 in an spheroid/Area of the spheroid) and analyzed the results using GraphPad Prism.

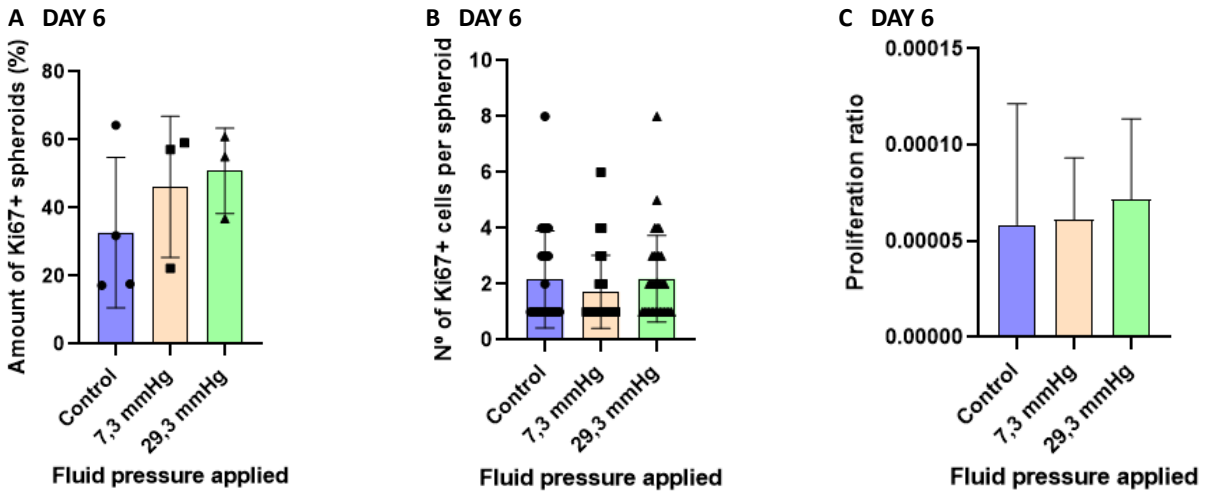

Fig. 12: A: Graph showing the amount of Ki67 positive spheroids for each chip analyzed under each condition on day 6 after seeding. Statistical analyses were performed using one-way ANOVA test followed by Tukey's

multiple comparisons test. n=10 (4 control chips, 3 chips under an IFP of 7.3 mmHg and 3 chips under an IFP of 29.3 mmHg). n.s. not significant. Data are means ± SD. **B**: Graph showing the number of cells positive for Ki67 for each positive spheroid analyzed under each condition on day 6 after seeding. Statistical analyses were performed using Kruskal-Wallis test followed by Dunn's multiple comparisons test. n=81 (24 control spheroids, 25 spheroids under an IFP of 7.3 mmHg and 32 spheroids under an IFP of 29.3 mmHg). n.s. not significant. Data are means ± SD. **C**: Graph showing the proliferation ratio of Ki67 positive spheroids under each condition. Statistical analyses were performed using Kruskal-Wallis test followed by Dunn's multiple comparisons test. n=81 (24 control spheroids, 25 spheroids under an IFP of 7.3 mmHg and 32 spheroids under an IFP of 29.3 mmHg). n.s. not significant. Data are means ± SD. All graphs were created with GraphPad Prism 8.

As shown in **fig. 12** and **table 10** (annexes), there is a tendency of larger proportions of Ki67+ spheroids in microchips that were under a higher IFP on day 6 after seeding. However, no significant differences between means within each fluid pressure category were observed. Equally, no significant differences between the average number of Ki67+ cells per Ki67+ spheroid were observed. The vast majority of Ki67+ spheroids had between 1 and 4 Ki67+ cells, except for one or two spheroids on each category that showed higher values. In all cases, the spheroids that had a notably larger amount of Ki67+ cells (proliferative cells) were remarkably large (spheroid area $>10^4$ μm^2). In terms of proliferation ratios, the average proliferation ratio of spheroids under an IFP of 29.3 mmHg is slightly higher than that of spheroids under an IFP of 7.3 mmHg, and that one is slightly higher than that of control spheroids. Nevertheless, there are no significant differences among means according to the statistical analysis performed.

We also analyzed the average actin intensity of the spheroids through their mean gray value in the phalloidin channel (as explained in the image analysis section). We first quantified the mean phalloidin intensity of all spheroids analyzed and then, we selected the values of those spheroids that were positive for Ki67. Additionally, we made distribution graphs of spheroids according to their mean gray value at day 6 after seeding (**fig. 13** and **tables 11, 12 and 13** (annexes)). We noticed that spheroids with large mean gray values were those whose area was bigger and, frequently, contained a larger number of proliferative cells.

Contrary to what could be thought, spheroids under a high IFP (29.3 mmHg) did not show an average larger mean gray value than the rest of the spheroids, either when all spheroids were evaluated or just the ones with proliferative cells (**fig 13A and 13B**). However, the distribution of spheroids according to their mean gray value was not the same for each category. For example, while the number of spheroids under fluid pressure within the lowest mean gray value range was really low, a third of control spheroids had a mean gray value below 1000 (**fig. 13C**). This proportion decreases when analyzing Ki67+ spheroids only (**fig. 13D**).

No significant differences among the average mean gray value of spheroids grown under different IFP conditions were found, so we came to the conclusion that phalloidin intensity was mostly determined by the size of the spheroids rather than the IFP applied. It seems logical for large spheroids to have a higher amount of actin than small spheroids, as this protein plays a role in adherens and tight junctions, which provide contact between adjacent epithelial cells. A larger amount of cells involves a larger number of adherens and tight junctions within the spheroid and thus, higher actin intensity.

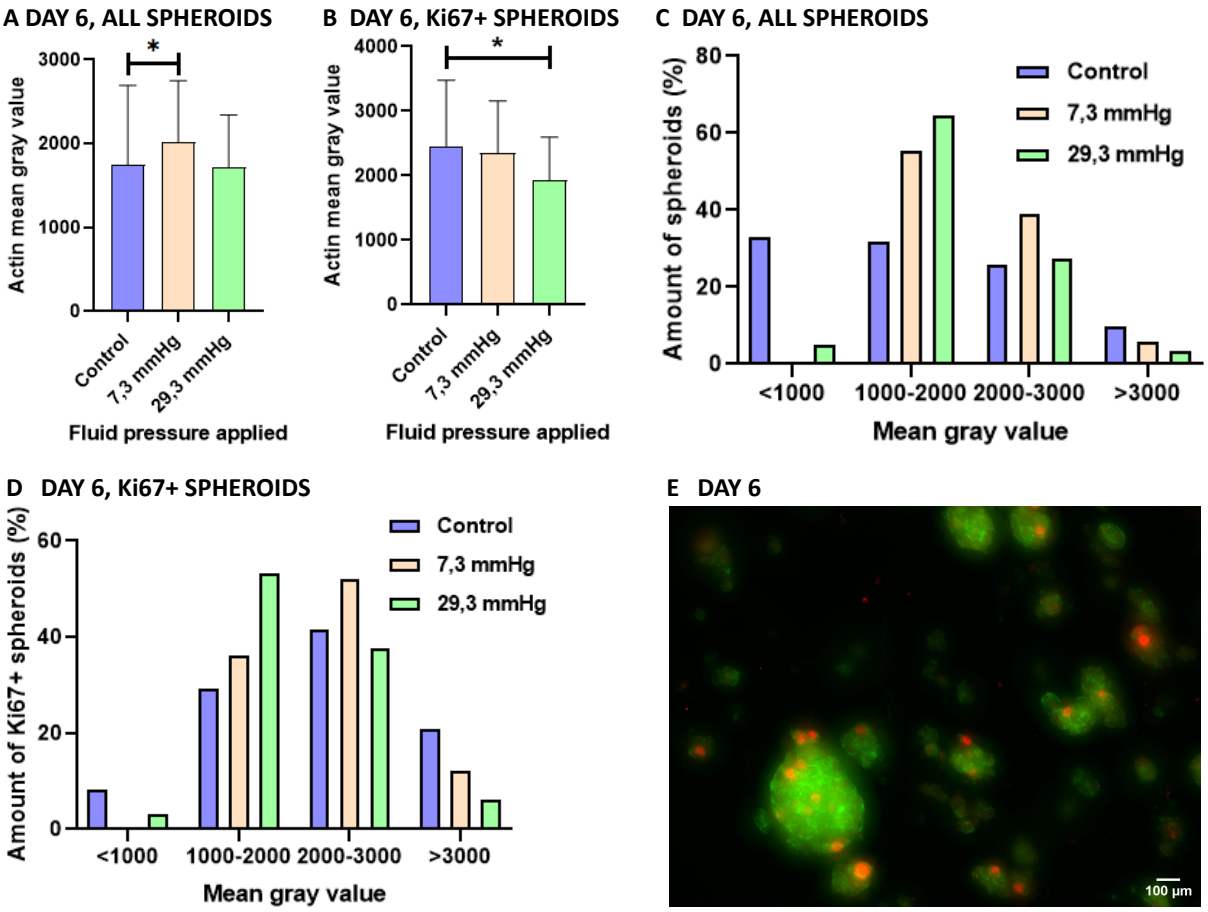

Fig. 13: **A**: Graph showing the average mean gray value in the phalloidin channel of all PANC-1 spheroids under different fluid pressure conditions on day 6 after seeding. Statistical analyses were performed using Kruskal-Wallis test followed by Dunn's multiple comparisons test. n=198 (82 control spheroids, 54 spheroids under an IFP of 7.3 mmHg and 62 spheroids under an IFP of 29.3 mmHg). P=0,0283. Data are means ± SD. **B**: Graph showing the average mean gray value in the phalloidin channel of all Ki67+ PANC-1 spheroids under different fluid pressure conditions on day 6 after seeding. Statistical analyses were performed using one-way ANOVA test followed by Tukey's multiple comparisons test. n=81 (24 control spheroids, 25 spheroids under an IFP of 7.3 mmHg and 32 spheroids under an IFP of 29.3 mmHg). P=0,0495. Data are means ± SD. **C**: Distribution graph of all PANC-1 spheroids analyzed according to their mean gray value on day 6 after seeding. Statistical analyses were performed using two-way ANOVA test followed by Tukey's multiple comparisons test. n=198 (82 control spheroids, 54 spheroids under an IFP of 7.3 mmHg and 62 spheroids under an IFP of 29.3 mmHg). n.s. not significant. Data are means ± SD. **D**: Distribution graph of all Ki67+ PANC-1 spheroids according to their mean gray value on day 6 after seeding. Statistical analyses were performed using two-way ANOVA test followed by Tukey's multiple comparisons test. n=81 (24 control spheroids, 25 spheroids under an IFP of 7.3 mmHg and 32 spheroids under an IFP of 29.3 mmHg). n.s. not significant. Data are means ± SD. **E**: Fluorescence microscopy image of PANC-1 spheroids on day 6 after seeding showing phalloidin staining in green and Ki67 staining in red.

6.3. Fluid pressure applied to PDX cells embedded in a 4 mg/mL collagen hydrogel did not show conclusive results

In our last experiment, we wanted to recreate the conditions of the previous experiment with an established PDX cell line (354-gfp), as we thought that it would be interesting to check if a patient-derived cell line behaved similarly to PANC-1 cells under IFP. PDX models are acknowledged to be more accurate and clinically relevant as they conserve the biological features of the original tissue (42) . Compared to commercial cell lines grown *in vitro* like PANC-1, that show some genetic and epigenetic differences with regard to the original tissue, PDX models retain the original genetic

and phenotypic characteristics to a larger extent (43). Because of that, it is common to use PDX models for drug development and therapeutic efficacy evaluation.

On account of previous experiments carried out in the M2BE laboratory that are not related with this TFG, we knew that PDX 354-gfp cells grew optimally in a mixture of a solubilized basement membrane matrix secreted by Engelbreth-Holm-Swarm (EHS) mouse sarcoma cells (Matrigel® (Corning Inc.)) and collagen. Nevertheless, this mixture results in hydrogels that are more feeble than the ones based exclusively on collagen. In a first attempt, we carried out an experiment with three microchips (1 chip control and 2 chips where an IFP of 7.3 mmHg was applied). At the moment bright-field pictures were taken, we noticed that the hydrogel of the control chip was in good condition and we could appreciate cell growth, even though less spheroids had grown compared to the PANC-1 experiment. However, in the case of the devices under pressure, the hydrogel was not resistant enough to resist the mechanical stress due to the fluid pressure applied plus the manipulation required to assemble the 3D structures and it had pulled off the central chamber. Thus, for the following experiment we decided to cultivate PDX cells in a hydrogel with 4 mg/mL of collagen, just like we did for PANC-1 cells.

It was observed that the average area of PDX 354-gfp spheroids at day 1 after seeding was much smaller than the average area of PANC-1 spheroids at day 1 after seeding (approximately half the PANC-1 average area) (**table 14** (annexes)). Nonetheless, this cell line is extremely aggressive and growth ratio values for PDX spheroids were far larger than for PANC-1 spheroids (in some cases over a ratio of 15) and, consequently, PDX spheroid areas and PANC-1 spheroid areas were comparable at day 6 after seeding (**table 14** (annexes)).

Just like PANC-1 spheroids, PDX spheroids did not show significant differences among mean spheroid areas on day 1 after seeding (**fig. 14**). However, the results obtained at day 6 after seeding differed from the ones obtained for PANC-1 spheroids. As it can be seen in fig. 14, the average area for control spheroids and spheroids under an IFP of 29.3 mmHg was pretty similar, while the average area for spheroids under an IFP of 7.3 mmHg was considerably lower. The standard deviation values were significantly different between the three groups as well. These results can be explained because of a lack of time to repeat the experiment, we were only able to test two microchips under each condition, a sample size not big enough to come to a firm conclusion.

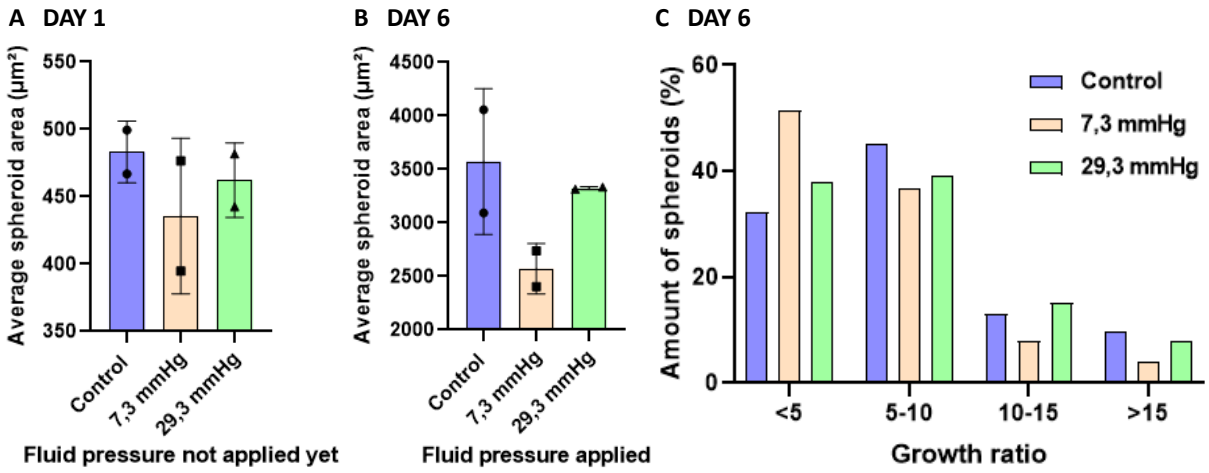

Fig. 14: **A**: Graph showing the average area of PDX control spheroids and spheroids under an interstitial fluid pressure of 7.3 mmHg and 29.3 mmHg at day 1 after seeding. Statistical analyses were performed using a

one-way ANOVA test followed by Tukey's multiple comparisons test. n=6 (2 chips per condition). n.s. not significant. Data are means ± SD. **B**: Graph showing the average area of PDX control spheroids and spheroids under an interstitial fluid pressure of 7.3 mmHg and 29.3 mmHg at day 6 after seeding. Statistical analyses were performed using one-way ANOVA test followed by Tukey's multiple comparisons test.n=6 (2 chips per condition). n.s. not significant. Data are means ± SD. **C**: Distribution graph of PDX spheroids according to their growth ratio at day 6 after seeding. Statistical analyses were performed using two-way ANOVA test followed by Tukey's multiple comparisons test. n=294 (93 control spheroids, 101 spheroids under an IFP of 7.3 mmHg and 100 spheroids under an IFP of 29.3 mmHg). n.s. not significant. Data are means ± SD. All graphs were created with GraphPad Prism 8.

As for growth ratios, no significant differences between means within growth ratio ranges were observed (**fig. 14**). The amount of control spheroids and spheroids under an IFP of 29.3 mmHg was pretty similar for all of the growth ratio ranges tested and there seemed to be a tendency of lower percentages of spheroids under a pressure of 7.3 mmHg as growth ratio increased.

Similarly to what we did for PANC-1 spheroids, we analyzed the distributions of spheroid areas at day 1 and 6 after seeding for all chips (**fig. 15** and **tables 15 and 16** (annexes)). Again, on day 1 after seeding (when pressure had not been applied yet) there were no significant differences within each range of area between the amount of spheroids that were later going to serve as controls or have a certain fluid pressure applied. No significant differences were observed on day 6 after seeding either. On day 6 after seeding, the majority of spheroids of any condition had an area between 10^3 and 6×10^3 µm² and more than half of the spheroids in which pressure had been applied had an area between 10^3 and 3×10^3 µm² (51,5% spheroids under an IFP of 7.3 mmHg and 53% spheroids under an IFP of 29.3 mmHg). The amount of spheroids under an IFP of 29.3 mmHg within the smallest range of area was the lowest, but there were more control spheroids within the largest range of area than spheroids under pressure (**fig. 15**).

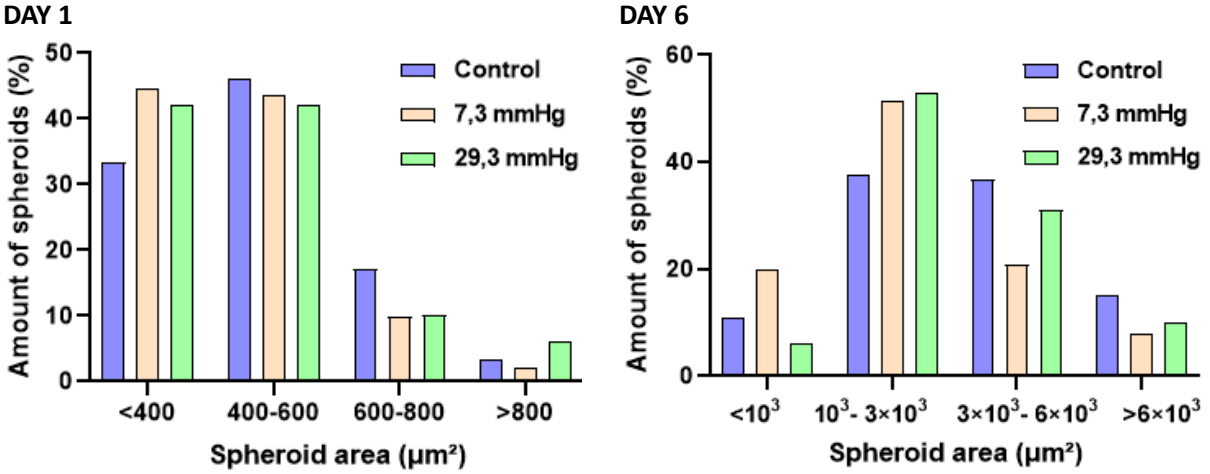

Fig. 15: Distribution graphs of PDX spheroids according to their areas at day 1 (left) and day 6 (right) after seeding. Statistical analyses were performed using two-way ANOVA test followed by Tukey's multiple comparisons test. n= 294 (93 control spheroids, 101 spheroids under an IFP of 7.3 mmHg and 100 spheroids under an IFP of 29.3 mmHg). n.s. not significant. Data are means ± SD. Graphs were created with GraphPad Prism 8.

In terms of morphology, we noticed that PANC-1 spheroids were rounder and more regular than PDX spheroids grown in a 4 mg/mL collagen matrix. Furthermore, PDX 354-gfp cells have a tendency to adhere to the surface, even in 3D cultures, and when they do so, they show a

fibroblast-like morphology. However, this tendency decreased when PDX spheroids were grown in a 4 mg/mL collagen hydrogel instead of in a Matrigel® and collagen mix.

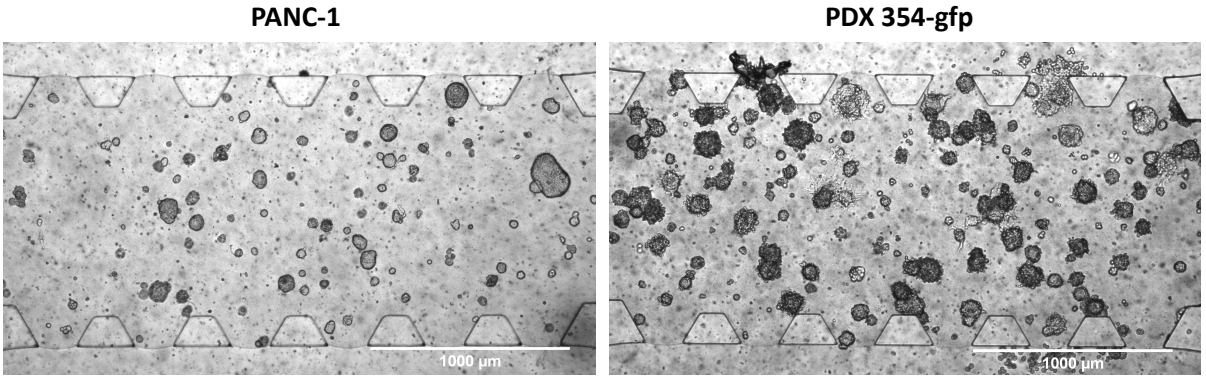

Fig. 16: Bright-field microscopy images of the central chamber of PANC-1 spheroids (no pressure applied) (left picture) and PDX 354-gfp spheroids (no pressure applied) (right picture), both embedded in a 4 mg/mL collagen hydrogel at day 6 after seeding.

6.4. An experiment using FITC-dextran indicates that chemotherapy drugs could reach tumor cells inside microchips under IFP using our 3D printed prototypes

In our last experiment we wanted to know if the effect of chemotherapy drugs could be tested over spheroids under IFP grown using our 3D printed system. In other words, we wanted to know if a solution containing chemotherapy drugs added to the syringes once the 3D structures were assembled could cover the whole length of the tubes and pass though one side of the hydrogel to another. For this purpose, we used 5 microchips attached to glass bottom dishes and filled with a 4 mg/mL collagen hydrogel. One of them served as control, two of them were placed at the base of prototypes with 10 cm columns and the rest were placed at the base of prototypes with 40 cm columns. The tubes were filled with PBS and a solution of 0,2 mg/mL FITC-dextran in PBS was added to two of the four syringes of each prototype (the ones connected to wells on the same side of the hydrogel). In the case of the control chip, the solution containing 0,2 mg/mL of FITC-dextran was added directly to two wells on the same side of the hydrogel.

FITC-dextran (4 KDa) has a higher molecular weight than common chemotherapy drugs used for PDAC treatment, like gemcitabine (293.2 Da), 5-fluorouracil (130 Da) or folfirinox (1585.5 Da) (44, 45). Dextran was conjugated with FITC (fluorescein isothiocyanate) so that we could evaluate if the solution reached the hydrogel and passed through it using a fluorescence microscope.

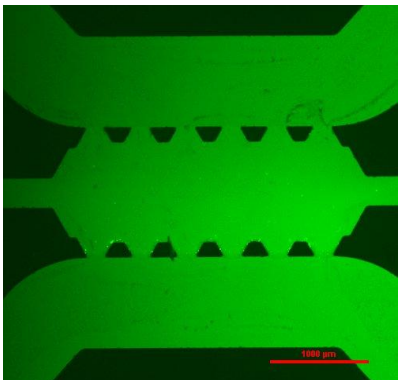

Fig. 17: Fluorescence microscopy image of the central chamber and the adjacent media channels of a microchip under an interstitial fluid pressure of 29.3 mmHg after a solution of 0,2 mg/mL of FITC-dextran in PBS had passed through one side of the hydrogel to the other.

A few hours later (approximately 3 hours for the chips placed at the base of the shorter columns and 4 hours for the chips placed at the base of the larger columns) we appreciated a light green coloration on all wells. The time required for this to occur on the control chip was 30 minutes. Then we dismantled the 3D structures and proceeded to the fluorescence microscopy observation. When illuminated with light of a wavelength of 495 nm, the central chamber of all microchips as well as the adjacent media channels turned green because of the presence of FITC (**fig. 17**). Thus, we proved that the FITC-dextran solution could pass through the tubes that connected the syringes with the microchip and through the pores of the hydrogel. Consequently, we think that chemotherapy drugs with a similar or smaller molecular weight would also be able to pass through the hydrogel pores and reach the cancerous cells grown in there.

7. CONCLUSIONS

1. We generated a pancreatic-on-a-chip model using different concentrations of extracellular matrix (collagen) for the 3D growth of human pancreatic cells. We observed that PANC-1 spheroids grown in microfluidic devices grow faster in with 4 mg/mL type I collagen matrix than in 6 mg/mL type I collagen, while spheroids grown in 6 mg/mL collagen have a slightly rounder and more regular shape than the ones grown in 4 mg/mL collagen.

2. We were able to create a safe, easy-to-use 3D printed system to induce interstitial fluid pressure in our pancreatic-on-a-chip model, in which a maximum IFP of 29.3 mmHg was exerted.

3. We noticed the effects of interstitial fluid pressure on the growth of pancreatic tumor spheroids at low (7.3 mmHg) and high IFP (29.3 mmHg). There was a tendency of larger areas for PANC-1 spheroids under low IFP versus control condition at day 6 after seeding and a significant difference between the area of control spheroids and the area of spheroids under the highest IFP applied.

4. Due to the differences in cell growth between control and pressure conditions we analyzed molecular parameters of PANC1 under those conditions. We found higher phalloidin intensity values and larger amounts of Ki67+ cells in larger PANC-1 spheroids, regardless of whether IFP was previously applied or not to the cultures. Nevertheless, as there appears to be a correlation between the final spheroid size and the IFP spheroids were subjected to, it would be interesting to repeat the experiments with a larger sample size to see if this tendency continues. If so, higher actin intensity values and more proliferative cells would be expected for spheroids under an IFP of 29.3 mmHg.

5. When analyzing if the interstitial fluid pressure effects observed in human pancreatic tumor spheroids derived from patients (PDX 354-gfp) was the same as with an established human tumor cell line we observed that the application of IFP over PDX 354-gfp cells did not come to a firm conclusion. This was due to the fact that the sample size of the experiment carried out was not big enough to be considered representative. Thus, in order to evaluate if the IFP effects seen in the established human tumor cell line PANC-1 are the same as with human pancreatic tumor spheroids derived from patients, more experiments are required.

6. Differences in spheroids size, growth rate and morphology between PANC-1 cells and PDX 354-gfp cells were observed. However, they appear to be due to the particular cell lines characteristics and not to the application of IFP over the cultures.

7. We observed that chemotherapy drugs frequently used for pancreatic cancer treatment could reach tumor cells grown in our microchips under IFP using our 3D printed system. This indicates that studying the effects of IFP over the tumor's chemoresistance in our pancreatic-on-a-chip model is possible.

8. BIBLIOGRAPHY

1. Rawla P, Sunkara T, Gaduputi V. Epidemiology of Pancreatic Cancer: Global Trends, Etiology and Risk Factors. World J Oncol 2019;10:10–27. https://doi.org/10.14740/WJON1166.
2. Pancreatic Cancer Prognosis | Johns Hopkins Medicine. n.d. https://www.hopkinsmedicine.org/health/conditions-and-diseases/pancreatic-cancer/pancreatic-cancer-prognosis (accessed August 15, 2023).
3. A-Kader HH, Ghishan FK. The Pancreas. Textbook of Clinical Pediatrics 2012:1925. https://doi.org/10.1007/978-3-642-02202-9_198.
4. Sayed SA El, Mukherjee S. Physiology, Pancreas. StatPearls 2023.
5. ¿Qué es el cáncer de páncreas? | American Cancer Society. n.d. https://www.cancer.org/es/cancer/tipos/cancer-de-pancreas/acerca/que-es-el-cancer-de-pancreas.html (accessed August 15, 2023).
6. Miquel M, Zhang S, Pilarsky C. Pre-clinical Models of Metastasis in Pancreatic Cancer. Front Cell Dev Biol 2021;9:748631. https://doi.org/10.3389/FCELL.2021.748631/BIBTEX.
7. Hanahan D, Weinberg RA. Hallmarks of cancer: the next generation. Cell 2011;144:646–74. https://doi.org/10.1016/J.CELL.2011.02.013.
8. Truffi M, Sorrentino L, Corsi F. Fibroblasts in the Tumor Microenvironment. Adv Exp Med Biol 2020;1234:15–29. https://doi.org/10.1007/978-3-030-37184-5_2.
9. Anderson NM, Simon MC. Tumor Microenvironment. Curr Biol 2020;30:R921. https://doi.org/10.1016/J.CUB.2020.06.081.
10. Truong LH, Pauklin S. Pancreatic Cancer Microenvironment and Cellular Composition: Current Understandings and Therapeutic Approaches. Cancers (Basel) 2021;13. https://doi.org/10.3390/CANCERS13195028.
11. Feig C, Gopinathan A, Neesse A, Chan DS, Cook N, Tuveson DA. The pancreas cancer microenvironment. Clin Cancer Res 2012;18:4266–76. https://doi.org/10.1158/1078-0432.CCR-11-3114.
12. Ferrara B, Pignatelli C, Cossutta M, Citro A, Courty J, Piemonti L. The Extracellular Matrix in Pancreatic Cancer: Description of a Complex Network and Promising Therapeutic Options. Cancers (Basel) 2021;13. https://doi.org/10.3390/CANCERS13174442.
13. Zhang YF, Jiang SH, Hu LP, Huang PQ, Wang X, Li J, et al. Targeting the tumor microenvironment for pancreatic ductal adenocarcinoma therapy. Chin Clin Oncol 2019;8:18–18. https://doi.org/10.21037/CCO.2019.03.02.
14. Ho WJ, Jaffee EM, Zheng L. The tumour microenvironment in pancreatic cancer — clinical challenges and opportunities. Nat Rev Clin Oncol 2020;17:527. https://doi.org/10.1038/S41571-020-0363-5.
15. Perez VM, Kearney JF, Yeh JJ. The PDAC Extracellular Matrix: A Review of the ECM Protein Composition, Tumor Cell Interaction, and Therapeutic Strategies. Front Oncol 2021;11:751311. https://doi.org/10.3389/FONC.2021.751311/BIBTEX.

16. Merali N, Chouari T, Kayani K, Rayner CJ, Jiménez JI, Krell J, et al. A Comprehensive Review of the Current and Future Role of the Microbiome in Pancreatic Ductal Adenocarcinoma. Cancers 2022, Vol 14, Page 1020 2022;14:1020. https://doi.org/10.3390/CANCERS14041020.
17. Elgundi Z, Papanicolaou M, Major G, Cox TR, Melrose J, Whitelock JM, et al. Cancer Metastasis: The Role of the Extracellular Matrix and the Heparan Sulfate Proteoglycan Perlecan. Front Oncol 2019;9:1482. https://doi.org/10.3389/FONC.2019.01482.
18. Basson MD, Zeng B, Downey C, Sirivelu MP, Tepe JJ. Increased extracellular pressure stimulates tumor proliferation by a mechanosensitive calcium channel and PKC-β. Mol Oncol 2015;9:513. https://doi.org/10.1016/J.MOLONC.2014.10.008.
19. Purkayastha P, Jaiswal MK, Lele TP. Molecular cancer cell responses to solid compressive stress and interstitial fluid pressure. Cytoskeleton 2021;78:312–22. https://doi.org/10.1002/CM.21680.
20. Heldin CH, Rubin K, Pietras K, Östman A. High interstitial fluid pressure — an obstacle in cancer therapy. Nature Reviews Cancer 2004 4:10 2004;4:806–13. https://doi.org/10.1038/nrc1456.
21. Provenzano PP, Cuevas C, Chang AE, Goel VK, Von Hoff DD, Hingorani SR. Enzymatic targeting of the stroma ablates physical barriers to treatment of pancreatic ductal adenocarcinoma. Cancer Cell 2012;21:418–29. https://doi.org/10.1016/J.CCR.2012.01.007.
22. Dufort CC, DelGiorno KE, Carlson MA, Osgood RJ, Zhao C, Huang Z, et al. Interstitial Pressure in Pancreatic Ductal Adenocarcinoma Is Dominated by a Gel-Fluid Phase. Biophys J 2016;110:2106. https://doi.org/10.1016/J.BPJ.2016.03.040.
23. Kapałczyńska M, Kolenda T, Przybyła W, Zajączkowska M, Teresiak A, Filas V, et al. 2D and 3D cell cultures – a comparison of different types of cancer cell cultures. Arch Med Sci 2018;14:910. https://doi.org/10.5114/AOMS.2016.63743.
24. Nordin AN, Abd Manaf A. Design and fabrication technologies for microfluidic sensors. Microfluidic Biosensors 2023:41–85. https://doi.org/10.1016/B978-0-12-823846-2.00004-3.
25. Özdemir BC, Pentcheva-Hoang T, Carstens JL, Zheng X, Wu CC, Simpson TR, et al. Depletion of Carcinoma-Associated Fibroblasts and Fibrosis Induces Immunosuppression and Accelerates Pancreas Cancer with Reduced Survival. Cancer Cell 2015;28:831–3. https://doi.org/10.1016/J.CCELL.2015.11.002.
26. Hosein AN, Dougan SK, Aguirre AJ, Maitra A. Translational advances in pancreatic ductal adenocarcinoma therapy. Nat Cancer 2022;3:272–86. https://doi.org/10.1038/S43018-022-00349-2.
27. Andersen LMK, Wegner CS, Simonsen TG, Huang R, Gaustad JV, Hauge A, et al. Lymph node metastasis and the physicochemical micro-environment of pancreatic ductal adenocarcinoma xenografts. Oncotarget 2017;8:48060–74. https://doi.org/10.18632/ONCOTARGET.18231.
28. Mandal A, Shahidullah M, Delamere NA. Hydrostatic Pressure–Induced Release of Stored Calcium in Cultured Rat Optic Nerve Head Astrocytes. Invest Ophthalmol Vis Sci 2010;51:3129. https://doi.org/10.1167/IOVS.09-4614.
29. Shang M, Lim S Bin, Jiang K, Yap YS, Khoo BL, Han J, et al. Microfluidic studies of hydrostatic pressure-enhanced doxorubicin resistance in human breast cancer cells. Lab Chip 2021;21:746–54. https://doi.org/10.1039/D0LC01103G.
30. Shin, Y., S. Han, J. S. Jeon, K. Yamamoto, I. K. Zervantonakis, R. Sudo, R. D. Kamm, and S. Chung. Microfluidic assay for simultaneous culture of multiple cell types on surfaces or within hydrogels. Nat. Protoc. 7:1247–1259, 2012.
31. Farahat, W. A. et al. Ensemble analysis of angiogenic growth in three-dimensional microfluidic cell cultures. PLoS One 7 (2012).

32. Plou J, Juste-Lanas Y, Olivares V, del Amo C, Borau C, García-Aznar JM. From individual to collective 3D cancer dissemination: roles of collagen concentration and TGF-β. Scientific Reports 2018 8:1 2018;8:1–14. https://doi.org/10.1038/s41598-018-30683-4.
33. Kanitthamniyom P, Zhang Y. Application of polydopamine in biomedical microfluidic devices. Microfluidics and Nanofluidics 2018 22:3 2018;22:1–13. https://doi.org/10.1007/S10404-018-2044-6.
34. Dabaghi M, Shahriari S, Saraei N, Da K, Chandiramohan A, Selvaganapathy PR, et al. Surface modification of PDMS-based microfluidic devices with collagen using polydopamine as a spacer to enhance primary human bronchial epithelial cell adhesion. BioRxiv 2020:2020.11.09.375709. https://doi.org/10.1101/2020.11.09.375709.
35. Holle AW, Kalafat M, Ramos AS, Seufferlein T, Kemkemer R, Spatz JP. Intermediate filament reorganization dynamically influences cancer cell alignment and migration. Sci Rep 2017;7. https://doi.org/10.1038/SREP45152.
36. ECACC General Cell Collection: 87092802 PANC-1. n.d. https://www.culturecollections.org.uk/products/celllines/generalcell/detail.jsp?refId=87092802&collection=ecacc_gc (accessed August 16, 2023).
37. Liu Y, Wu W, Cai C, Zhang H, Shen H, Han Y. Patient-derived xenograft models in cancer therapy: technologies and applications. Signal Transduction and Targeted Therapy 2023 8:1 2023;8:1–24. https://doi.org/10.1038/s41392-023-01419-2.
38. Kim H, Park CY, Lee JH, Kim JC, Cho CK, Kim HJ. Ki-67 and p53 expression as a predictive marker for early postoperative recurrence in pancreatic head cancer. Ann Surg Treat Res 2015;88:200. https://doi.org/10.4174/ASTR.2015.88.4.200.
39. Kopantzev E, Kondratyeva L, Kopantseva M, Kashkin K, Gnatenko D, Grigorieva E, et al. SOX9 Protein in Pancreatic Cancer Regulates Multiple Cellular Networks in a Cell-Specific Manner. Biomedicines 2022;10. https://doi.org/10.3390/BIOMEDICINES10071466/S1.
40. Charoen KM, Fallica B, Colson YL, Zaman MH, Grinstaff MW. EMBEDDED MULTICELLULAR SPHEROIDS AS A BIOMIMETIC 3D CANCER MODEL FOR EVALUATING DRUG AND DRUG-DEVICE COMBINATIONS. Biomaterials 2014;35:2264. https://doi.org/10.1016/J.BIOMATERIALS.2013.11.038.
41. Calori IR, Alves SR, Bi H, Tedesco AC. Type-I Collagen/Collagenase Modulates the 3D Structure and Behavior of Glioblastoma Spheroid Models. ACS Appl Bio Mater 2022;5:723–33. https://doi.org/10.1021/ACSABM.1C01138/SUPPL_FILE/MT1C01138_SI_001.PDF.
42. Koga Y, Ochiai A. Systematic Review of Patient-Derived Xenograft Models for Preclinical Studies of Anti-Cancer Drugs in Solid Tumors. Cells 2019;8. https://doi.org/10.3390/CELLS8050418.
43. Huo KG, D'Arcangelo E, Tsao MS. Patient-derived cell line, xenograft and organoid models in lung cancer therapy. Transl Lung Cancer Res 2020;9:2214. https://doi.org/10.21037/TLCR-20-154.
44. Principe DR, Underwood PW, Korc M, Trevino JG, Munshi HG, Rana A. The Current Treatment Paradigm for Pancreatic Ductal Adenocarcinoma and Barriers to Therapeutic Efficacy. Front Oncol 2021;11:688377. https://doi.org/10.3389/FONC.2021.688377/BIBTEX.
45. Chemotherapy Drugs Used in Pancreatic Cancer|Pancreatic Cancer Action. n.d. https://pancreaticcanceraction.org/about-pancreatic-cancer/treatment-options-for-pancreatic-cancer/treating-pancreatic-cancer/chemotherapy-for-pancreatic-cancer/chemotherapy-drugs-for-pancreatic-cancer/ (accessed August 16, 2023).